Atomistic simulations of the effect of Coulombic interactions on carrier fluctuations in doped silicon

Zudian Qin and Scott T. Dunham
Department of Electrical Engineering, University of Washington, Seattle, Washington 98195, USA
(Received 5 September 2003; published 10 December 2003)

Carrier distributions associated with point charges in silicon are calculated via the quantum perturbation method and used to determine Coulombic interactions between charged defects in the presence of carrier screening. The resulting interactions are used in kinetic lattice Monte Carlo simulations of defect-mediated diffusion to study dopant redistribution and associated variations in carrier concentration. Over a broad range of doping concentrations, Coulombic repulsion between like dopants leads to ordering, resulting in a more uniform electrical potential distribution (and therefore reduced threshold voltage variations) compared with random doping, the standard condition assumed in previous doping fluctuation analyses.

DOI: 10.1103/PhysRevB.68.245201 PACS number(s): 66.30.Pa, 85.30.−z, 87.53.Wz

Fluctuations in carrier density associated with discrete dopant atoms have been identified as a critical issue in controlling threshold voltage (V_{th}) in nanoscale metal-oxide-semiconductor field-effect transistors (MOSFET's).[1–3] To date, analysis of this phenomenon has largely assumed that the dopants are distributed randomly within the active region.[4–8] However, interactions between dopants during device fabrication can lead to correlations in dopant locations, modifying the resulting V_{th} variations. One source of these correlations is the Coulombic interactions between ionized dopants, screened by nearby free carriers. In this paper, we examine the effect of these interactions on variations in electrical potential within doped regions via kinetic lattice Monte Carlo (KLMC) simulations[9–11] which simultaneously solve for free carrier distributions and include the effect of associated potential variations on the diffusion of charged dopants and point defects.

To study doping fluctuations, a tool must first be capable of tracking dopant locations within the system. Traditional continuum simulators lack such capability since they focus on macroscopic-level averages (e.g., dopant concentrations) within the system without giving any information on locations of individual atoms. Kinetic lattice Monte Carlo simulations, on the other hand, are well suited to this task. The KLMC simulations utilized in this work operate on a silicon (diamond) lattice structure with impurities and point defects mapped to lattice sites.[9–11] The system evolves through transitions from one atomic configuration to the next, by virtue of point defect migration and reactions. The rates of these transitions are determined by the migration barriers combined with changes in system energy associated with transitions:

$$\nu = \nu_0 \exp\left(\frac{-E_m}{k_B T}\right)\exp\left(\frac{E_i - E_f}{2k_B T}\right), \tag{1}$$

where E_m is the unbiased migration barrier, E_i and E_f are the system energies before and after the transition, and T is the system temperature. The system energies are calculated based on the atomic arrangements of impurities and defects, with parameters from *ab initio* calculations and/or experimental observations. At each simulation step, one transition is chosen from the possible set based on the relative rates, and the system time is advanced by the inverse of the sum of the rates. By only considering transitions (and not lattice vibrations) associated with defects and impurities present in the system, the KLMC method overcomes the time-scale limits associated with molecular dynamics to consider macroscopic system and processing time scales.

As a result of the pointlike nature of charges associated with ionized dopants and statistical variations in local doping density, the electrical potential varies within the system (even for a region which is nominally homogeneous). These variations affect the dopant redistribution in two key ways: (i) ionized dopant atoms as well as charged point defects experience electrical fields due to the spatial variation in the potential and (ii) the population of point defects, which mediate dopant diffusion, depends on the local potential level. Traditionally, the free carrier concentrations and associated electrical potential have been calculated from dopant profiles using the charge neutrality assumption. However, at the atomic scale dopant atoms are discrete and nearly point like, and thus dopant concentration is no longer a valid measure. To obtain free carrier concentrations, we are forced to solve the Poisson equation in the presence of discrete point charges.

To clearly define the problem, we consider a system with a locally uniform background carrier (electron or hole) concentration. To maintain charge neutrality in the region, an equal but oppositely charged dopant (donor or acceptor) concentration is also assumed. A pair of charges is then introduced into the system with the positive (negative) charge held at the origin (point like) and the other mobile, negative (positive) charge released in the system. The challenge is then to solve the redistribution of mobile charges in the neighborhood of the point charge at the origin under consideration of the background carrier screening.

There exists a classical solution to the problem, best known in its potential form as the screened Coulomb potential. The classical approach applies Boltzmann statistics and assumes the validity of linearization of the Boltzmann equation.[12] The induced charge distribution has the same form as the screened Coulomb potential,

$$\rho(r) = \frac{-e}{4\pi L_D^2 r}\exp\left(-\frac{r}{L_D}\right), \tag{2}$$

 ©2003 The American Physical Society

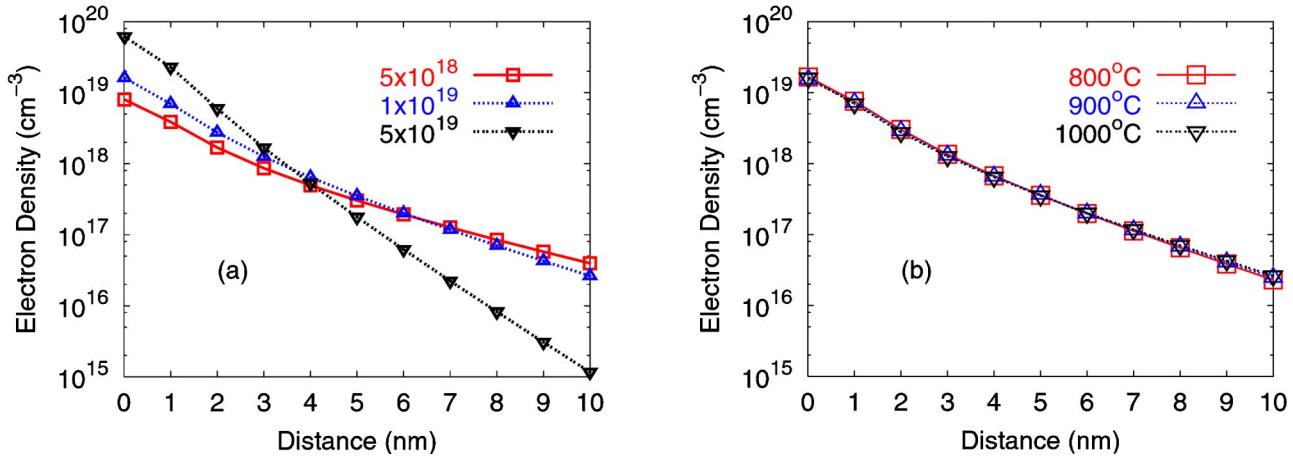

FIG. 1. Excess electron distributions in the neighborhood of a positive point charge, calculated using quantum perturbation method for (a) three distinct background carrier (electron) concentrations of 5×10^{18}, 1×10^{19}, and 5×10^{19} cm^{-3} at temperature of 1000 °C, and (b) three different system temperatures of 800, 900, and 1000 °C with the background carrier (electron) concentration set to 10^{19} cm^{-3}. As the carrier concentration increases, the distribution profile drops off more rapidly due to stronger screening. In contrast, the profiles show little dependence on temperature.

where L_D is the Debye length:

$$L_D = \sqrt{\frac{k_{Si}\varepsilon_0 k_B T}{e^2(n+p)}}. \tag{3}$$

Here, n and p are the background carrier concentrations. This solution has a simple analytic form, but diverges as r approaches zero, which is physically incorrect and causes problems with the carrier concentration derivation. To overcome this characteristic of the classical solution, a quantum approach is necessary.

In order to solve the problem in a practical way, two assumptions are made. The first assumption regards the system. We assume that the conduction band has a parabolic shape near its minima and conduction electrons are free. The second assumption is made on the approach, where we assume the quantum perturbation method is applicable to this problem.[13] Based on these two assumptions, the generalized susceptibility of the system, characterizing the system's response to an external sinusoidal perturbation, can be calculated as a function of spatial frequency of the perturbation:[14]

$$\chi(\vec{q}) = -\frac{6m_e^*}{\pi^3\hbar^2}\int \frac{f(E_{\vec{k}})}{2\vec{k}\cdot\vec{q}+q^2}d^3\vec{k}, \tag{4}$$

where q represents the spatial frequency of the sinusoidal perturbation, m_e^* is the effective mass of electrons $(0.33m_e)$, and the factor of 6 accounts for multiple conduction band minima. The background carrier concentration and system temperature enter as parameters through $f(E_{\vec{k}})$, the Fermi-Dirac distribution function, with the Fermi energy chosen to match the defined background carrier concentration. Equation (4) characterizes the response of conduction electrons. Had the response of holes been sought, m_e^* must be replaced by the hole effective mass m_h^* $(0.51m_e)$ and the factor of 6 changes to 2. Note that the effective masses are based on equivalent spherically symmetric extrema. We have repeated the calculations using heavy and light holes with nearly identical results.

Equation (4) describes the system's response to a sinusoidal perturbation. A perturbation consisting of a point charge has uniform components at all spatial frequencies, and the induced charge distribution can be integrated as[14,15]

$$\rho(\vec{r}) = e\int\left[\frac{k_{Si}\varepsilon_0}{\epsilon(\vec{q})}-1\right]\exp(i\vec{q}\cdot\vec{r})\frac{d^3\vec{q}}{(2\pi)^3}, \tag{5}$$

where $\varepsilon(\vec{q})$ is the dielectric function of the system:

$$\varepsilon(\vec{q}) = k_{Si}\varepsilon_0 - \frac{e^2}{q^2}\chi(\vec{q}). \tag{6}$$

Equation 5 was evaluated numerically and the results are depicted in Fig. 1. Figure 1(a) shows results for three distinct background carrier concentrations: 5×10^{18}, 1×10^{19}, and 5×10^{19} cm^{-3}. Clearly, the charge distribution drops off more rapidly with an increasing background carrier concentration, indicating a stronger screening effect. Figure 1(b) shows results for systems with temperatures of 800, 900, and 1000 °C, respectively. As seen, within the process temperature regime, the charge distribution depends only weakly on temperature.

Upon examination of numerical results for different background carrier concentrations and temperatures, we find that the quantum solution can be accurately modeled by

$$\rho(r) = \rho(0)\frac{r_0}{\sqrt{r^2+r_0^2}}\exp\left(-\frac{r}{L_D}\right), \tag{7}$$

where L_D is the classical Debye length by Eq. (3), r_0 is a parameter representing best fitting to the numerical results, and $\rho(0)$ is determined by the normalization condition. In fact, r_0 is nearly independent of temperature and is only a

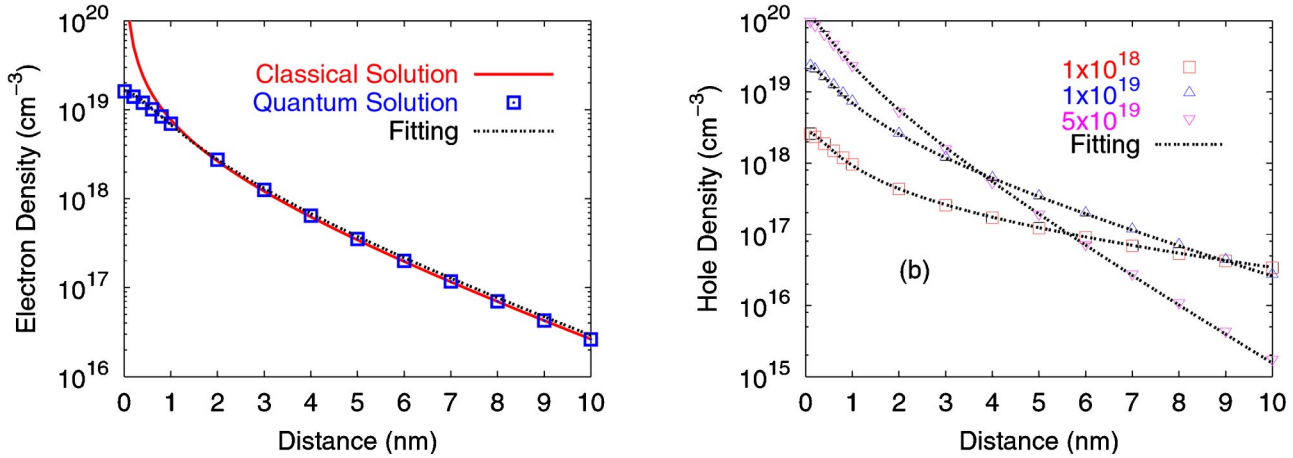

FIG. 2. (a) Excess electron distributions in the neighborhood of a positive point charge from both the classical and quantum solutions for a system with a background carrier (electron) concentration of 10^{19} cm^{-3} and a temperature of 1000 °C. The classical Debye length in this case is 2.67 nm. Also plotted is the fitting curve $1.48\times10^{19}\exp(-r/2.67)\times0.8/\sqrt{r^2+0.8^2}$, which shows excellent agreement with the quantum solution over the entire range. (b) Excess hole distributions in the neighborhood of a negative point charge for three (p-type) background doping levels at 1000 °C. The fitting curves are plotted using Eq. (7) with $r_0=0.40+0.021\ln(p/10^{18})$ nm and $\rho(0)$ from the normalization requirement.

weak function of background carrier concentrations. It can be represented as $0.65+0.065\ln(n/n_0)$ nm for n-type background doping and $0.40+0.021\ln(p/n_0)$ nm for p-type background doping, with $n_0=10^{18}$ cm^{-3}.

In Fig. 2(a), quantum and classical solutions are compared. The quantum solution deviates strongly from the classical solution at short range ($<1-2$ nm). Most significantly, it gives a finite value at the origin, where the classical solution diverges. The quantum solution parallels the classical solution at long range, but is 15%–20% higher due to the reduction in compensating charge near the ion. Equation (7) shows excellent agreement with the quantum solution over the entire range. Figure 2(b) shows quantum solutions for excess hole concentration in the neighborhood of a negative point charge for three different background doping levels, with fitting curves matching solutions in all cases. All previous calculations are carried out over background carrier concentrations up to 3×10^{20} cm^{-3}. Beyond this concentration limit, Friedel oscillations[16] characteristic of a metal appear and Eq. (7) no longer accurately predicts the numerical results.

Given the solution for the charge distribution in the neighborhood of a single point charge, the overall carrier concentration can be approximated by summing contributions from all ionized dopant atoms and charged defects, with a positive point charge (e.g., an ionized donor) inducing an electron cloud in its neighborhood and a negative charge (e.g., an ionized acceptor) inducing a hole cloud. The calculation of carrier distributions over the whole system is an iterative process, since the Debye length appearing in Eq. (7) is itself a function of local carrier concentrations [Eq. (3)]. Initially,

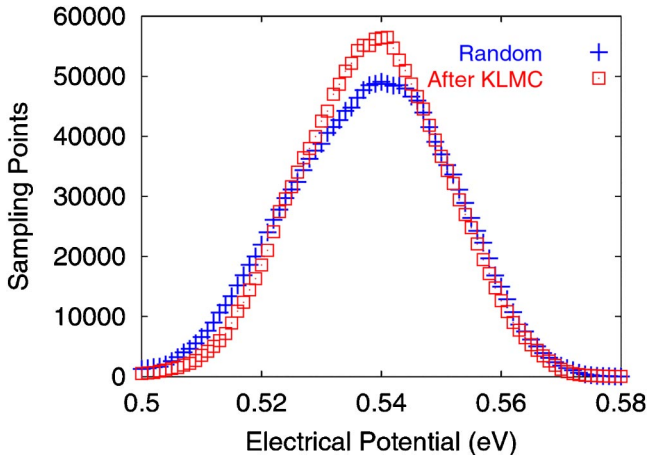

FIG. 3. Histogram over lattice sites (2×10^4) of the electrical potential before and after annealing at 1000 °C. Annealing leads to a narrower potential distribution, indicating effect of dopant-dopant repulsion on the dopant redistribution.

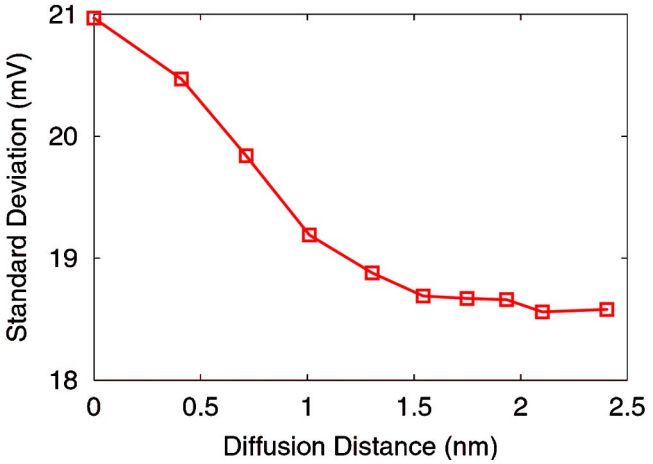

FIG. 4. Evolution of the standard deviation of the potential distribution vs diffusion distance ($\sqrt{Dt}$) for a doping level of 3×10^{19} cm^{-3}. The time constant for homogenization corresponds to a diffusion distance which varies from about 0.7 nm at 10^{20} cm^{-3} to 1.4 nm at 10^{19} cm^{-3}. The diffusion distance for homogenization is nearly independent of annealing temperature and is significantly less than the expected junction depths.

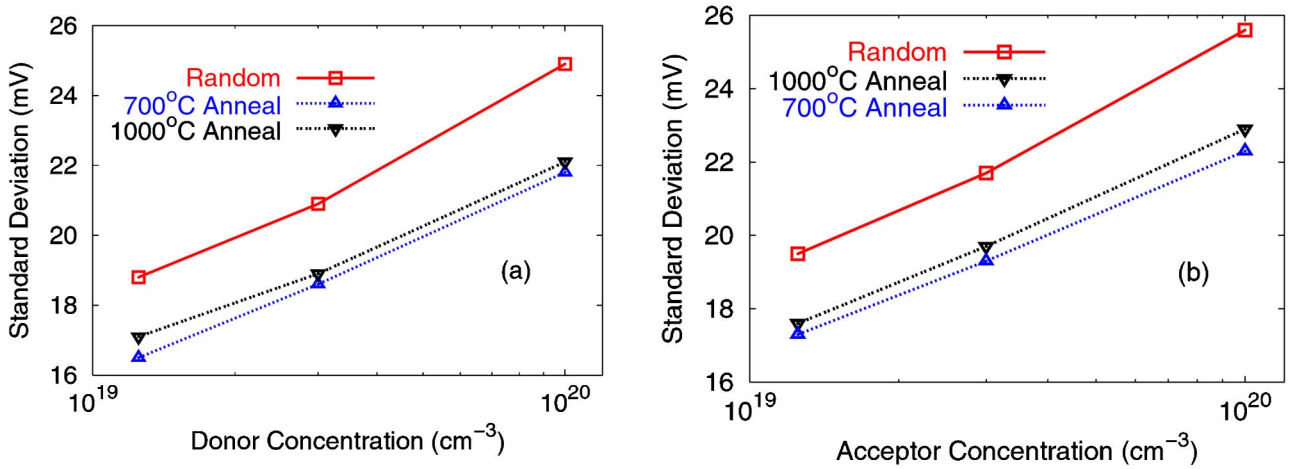

FIG. 5. Standard deviation of electron potential vs concentrations for (a) donor and (b) acceptor doping before and after annealing at 700 or 1000 °C. The distribution is broader for higher doping due to more sharply peaked carrier distribution screening dopants and for higher temperature due to the stronger role of entropy. However, in all cases, annealing shows a significant narrowing of the potential distribution attributed to Coulombic interactions between charged dopants. Differences between donor and acceptor doping arises from differences in conduction and valence band structures.

the carrier concentration is set equal to the dopant concentration averaged over a broad region. The Debye length is then calculated using Eq. (3) and the carrier concentration recalculated using Eq. (7). Subsequent iterations use the local carrier concentration to recalculate the Debye length, continuing until the carrier concentrations converge. The effective local electrical potential for use in the KLMC diffusion simulation is then derived from the carrier concentrations via the Boltzmann equation.

To analyze the effect of Coulombic interactions on doping fluctuations, dopant atoms are first randomly initialized in the system. The initial carrier densities and associated potential distribution are evaluated at room temperature (27 °C). The system is then annealed within the KLMC framework at an elevated temperature. After annealing, the potential distribution is reevaluated at 27 °C. During the annealing process, the carrier and potential distributions are calculated for the annealing temperature after each simulation step to reflect the evolved system configuration with current locations of charged defects and/or ionized dopant atoms. Figure 3 compares histograms of the potential distribution within the system, one for the initial random doping and the other after annealing. Notice that the system has a narrower potential distribution after annealing. We attribute this to dopant-dopant repulsion leading to a more uniform dopant distribution (ordering). In confirmation, no narrowing in the potential distribution is observed if the effect of the potential on dopant diffusion is neglected.

The extent of potential variations within the system can be characterized in terms of its standard deviation. Figure 4 depicts the evolution of this characteristic as a function of diffusion distance for a system under annealing. The diffusion distance required to achieve homogenization in the system varies from 1.4 nm to 0.7 nm over doping concentrations from 10^{19} to 10^{20} cm^{-3}. These values are all significantly less than the expected junction depths of future devices [4–6 nm for the 22 nm technology node based on the International Technology Roadmap for Semiconductors (ITRS) (Ref. 17)], and thus the full effect can be expected to be routinely observed. Figure 5 shows results from simulations on both *n*-type and *p*-type systems annealed at 700 and 1000 °C. In all cases, we observed reduced standard deviation of potential distributions after annealing. As would be expected, narrower potential distributions are achieved for both lower-temperature anneals and lower-doping-concentration systems. Lower temperatures lead to stronger ordering, as Coulombic repulsion is more effective compared to random hopping. Lower doping levels result in longer Debye lengths [Eq. (3)], so the potential varies less sharply around each dopant. Small differences are seen between *n*-type and *p*-type materials, arising from the differences in density of states and effective mass. The conduction band having more extrema with larger curvature results in lower values of *k* for occupied states and thus weaker variations in carrier density.

The KLMC simulation results reported above assumed that the dopant-interstitial pairs remained charged. However, for high doping levels, neutral dopant-interstitial pairs (dopant paired with oppositely charged defect) dominate diffusion.[18] We repeated our simulations assuming neutral pairs and found that the narrowing of the Fermi level (or carrier concentration) distribution was the same as for charged pairs (charged dopant paired with neutral defect), but that about 3–5 times more diffusion was required to order the dopant distribution. This suggests that the system may be reaching an equilibrium ordering at the simulation temperature.

In conclusion, we use a quantum perturbation calculation within the effective mass approximation to determine the carrier distribution in the neighborhood of a point charge in silicon. The resulting distribution is effectively modeled by a simple analytical expression which can be expected to find application in future nanoscale process and device simulations. KLMC simulations based on this model have shown that Coulombic interactions between like dopants causes or-

dering during annealing, resulting in a more uniform electrical potential distribution within the active region compared to the standard approach with random dopant placement. This leads to smaller variations in the threshold voltage, enabling further device scaling. Since lower temperatures give stronger ordering, low-T annealing may be used to further reduce V_{th} variations, since the thermal budget required for ordering is small compared to projected junction depths.

This work was supported by the Semiconductor Research Cooperation. Many of the calculations were conducted using a computing cluster donated by Intel.

[1] B. Hoeneisen and C.A. Mead, Solid-State Electron. **15**, 819 (1972).
[2] R.W. Keyes, Proc. IEEE **63**, 740 (1975).
[3] T. Mizuno, J. Okamura, and A. Toriumi, IEEE Trans. Electron Devices **41**, 2216 (1994).
[4] A. Asenov, G. Slavcheva, A.R. Brown, J.H. Davies, and S. Saini, IEEE Trans. Electron Devices **48**, 722 (2001).
[5] N. Sano and M. Tomizawa, Appl. Phys. Lett. **79**, 2267 (2001).
[6] I.D. Mayergoyz and P. Andrei, J. Appl. Phys. **90**, 3019 (2001).
[7] Y. Yasuda, M. Takamiya, and T. Hiramoto, IEEE Trans. Electron Devices **47**, 1838 (2000).
[8] X. Tang, V.K. De, and J.D. Meindl, IEEE Trans. VLSI Syst. **5**, 369 (1997).
[9] S.T. Dunham and C.D. Wu, J. Appl. Phys. **78**, 2362 (1995).
[10] M.M. Bunea and S.T. Dunham, in *Semiconductor Process and Device Performance Modeling*, edited by S. T. Dunham, C. D. Wilson, and J. Nelson, Mater. Res. Soc. Symp. Proc. No. **490** (Materials Research Society, Pittsburgh, 1998), pp. 3–8.
[11] Z. Qin and S.T. Dunham, in *Silicon Front-End Junction Formation Technologies*, edited by D.F. Downey, M.E. Law, A.P. Claverie, and M.J. Rendon, Mater. Res. Soc. Symp. Proc. No. **717** (Materials Research Society, Pittsburgh, 2002), p. C3.8.
[12] N.W. Ashcroft and N.D. Mermin, *Solid State Physics* (Holt, Rinehart and Winston, New York, 1976), p. 342.
[13] J.J. Sakurai, *Modern Quantum Mechanics* (Addison-Wesley, Reading, Massachusetts, 1994), pp. 285–298.
[14] J. Chazalviel, *Coulumb Screening by Mobile Charges: Applications to Materials Science, Chemistry, and Biology* (Birkhäuser, Boston, 1998), pp. 27–34.
[15] C. Kittle, *Introduction to Solid State Physics* (Wiley, New York, 1996), pp. 280–285.
[16] J. Friedel, Nuovo Cimento, Suppl. **7**, 287 (1958).
[17] *International Technology Roadmap for Semiconductors: Front End Processes* (ITRS, 2001), p. 24.
[18] P.M. Fahey, P.B. Griffin, and J.D. Plummer, Rev. Mod. Phys. **61**, 289 (1989).